arXiv:1609.02999v1 [cond-mat.mes-hall] 10 Sep 2016

Visualization of Au Nanoparticles Buried in a Polymer Matrix by Scanning Thermal Noise Microscopy

Atsushi Yao, Kei Kobayashi,* Kuniko Kimura, Shunta Nosaka, and Hirofumi Yamada

Department of Electronic Science and Engineering,

Kyoto University, Katsura, Nishikyo, Kyoto, 615-8510, Japan

(Dated: September 13, 2016)

Abstract

We demonstrated visualization of Au nanoparticles buried 300 nm into a polymer matrix by measurement of the thermal noise spectrum of a microcantilever with a tip in contact to the polymer surface. The subsurface Au nanoparticles were detected as the variation in the contact stiffness and damping reflecting the viscoelastic properties of the polymer surface. The variation in the contact stiffness well agreed with the effective stiffness of a simple one-dimensional model, which is consistent with the fact that the maximum depth range of the technique is far beyond the extent of the contact stress field.

PACS numbers: 07.79.Lh, 81.07.Lk, 46.35.+z, 81.05.Qk

Several researchers have recently demonstrated visualization of subsurface features with a nanometer-scale resolution using various imaging schemes based on atomic force microscopy (AFM) [1–19]. As the maximum depth range of the technique reaches on the order of one micrometer and the potential applications include those in the industrial, biological and medical research fields, much attention has been paid to these techniques. However, the imaging mechanisms and underlying physics are still not well understood. This is partly because all the schemes used for subsurface imaging require excitation of the oscillation of the cantilever and/or sample surface, and the key factors contributing to the subsurface contrasts could vary depending on the imaging schemes.

One of the major imaging schemes is to excite two piezoelectric actuators located at the cantilever base and the bottom of the sample at two different frequencies and detect the flexural oscillation of the cantilever at the beat frequency, which is caused by the nonlinear tip-sample interaction [3–5, 8, 10–12]. The beat frequency is tuned at the contact resonance frequency (f_c) of the cantilever to enhance the contribution of the nonlinear coupling to the imaging mechanism as well as the signal-to-noise ratio. The technique is referred to as heterodyne force microscopy (HFM) or scanning near-field ultrasound holography (SNFUH). It has been applied to subsurface imaging for various sample systems with a depth range of a few hundred nm, but mainly for buried hard objects in a soft matrix. The imaging mechanism by this scheme has been explained as the amplitude and phase modulation of the surface acoustic standing wave resulting from the interference of the ultrasound waves transmitted through the sample and cantilever [3, 20].

Another possible imaging scheme is to excite a piezoelectric actuator located at the bottom of the sample at a frequency close to f_c and detect the flexural oscillation of the cantilever at f_c. The technique is referred to as atomic force acoustic microscopy (AFAM) [21, 22]. Several researchers also reported visualization of subsurface features with a depth range of a few hundred nm by AFAM, of whose imaging mechanism was explained by the modulation of the contact stiffness due to the subsurface features [7, 23]. They also found that the result was consistent with a finite element analysis.

We have also demonstrated visualization of Au nanoparticles buried 900 nm in a polymer matrix using HFM and AFAM [15]. We recently measured the contact resonance spectra of the cantilever while the tip was scanned over the surface by sweeping the frequency of the sample excitation at each pixel. Since the contact resonance spectra were not skewed, they

were well fitted by the simple harmonic oscillator (SHO) model. We found that the contact resonance spectrum was affected by the Au nanoparticle underneath, and we concluded that the variation in the contact stiffness and damping was playing a major role in making subsurface contrasts in the AFAM images, while the tip-sample nonlinearity does not seem to significantly contribute [24].

As already mentioned, most of the subsurface imaging experiments have been based on the detection of the cantilever oscillation close to f_c. We now believe that the contact resonance is playing a major role in producing the subsurface contrasts in the AFAM, at least for the solid nanoparticles buried in a soft matrix. We then raised the question; do we really need to excite a cantilever oscillation? If we just need to measure the contact resonance spectra on the surface for subsurface imaging, it should be possible to do the same thing with the thermal drive of the cantilever. This was the motivation of the study.

There have been several reports about the AFM measurements of the tip-sample interactions using thermally driven cantilevers [25–30]. Motivated by the above question and inspired by these previous studies, we measured the thermal noise spectra of a cantilever on the polymer matrix with buried Au nanoparticles by introducing scanning thermal noise microscopy (STNM), which simply collects the contact resonance spectra of the cantilever at each pixel while the tip was scanned over the surface.

In this letter, we demonstrate visualization of the Au nanoparticles buried 300 nm in a polymer matrix by STNM. Since STNM does not require additional excitation methods of the cantilever base or sample surface, the contact resonance spectrum measured by STNM is free from the spurious peaks that hinder quantitative estimation of the contact stiffness and damping, and the nonlinear tip-sample interaction can be minimized because of a very small oscillation amplitude. We quantitatively evaluated the differences in the contact stiffness and damping of the polymer surface areas with and without the Au nanoparticle underneath using a linear spring dashpot model, and discuss the imaging mechanisms by STNM as well as those by other schemes.

Figure 1 shows a schematic of a sample's structure and the experimental setup of the STNM. We used a model sample of Au nanoparticles buried in a polymer matrix [15]. Au nanoparticles with diameters of 40 nm dispersed in water with a concentration of 0.006–0.007 wt% (Tanaka Kikinzoku Kogyo) were dropped onto a 125-μm-thick polyimide sheet (DuPont–Toray: Kapton 500V). The sheet was dried on a hot plate heated at 105°C. A

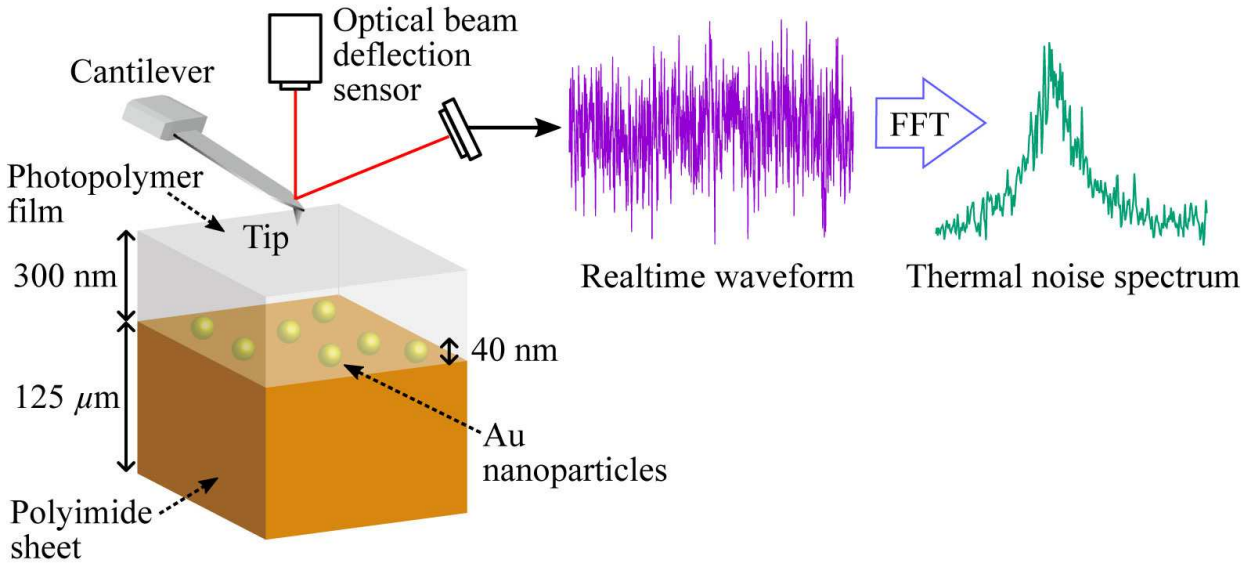

FIG. 1: Schematic of sample structure and experimental setup of scanning thermal noise microscopy (STNM). Au nanoparticles were deposited on a polyimide sheet, which were subsequently covered with a 300-nm-thick photopolymer film (see Ref. [15] for more details). While the tip was scanning the surface with a constant loading force, a realtime waveform of the cantilever deflection was recorded at each pixel. The thermal noise spectrum was calculated by the fast Fourier transform algorithm (FFT).

photopolymer (Rohm and Haas: S1813G) was spin-coated as the top-coat and the sheet was annealed at 150°C for 5 min. The thickness of the top-coat layer was determined by a stylus profiler (KLA–Tencor: P–15) to be about 300 nm. More details about the sample preparation procedures and a cross-sectional scanning electron micrograph were published in Ref. [15].

We used a commercial AFM (JEOL: SPM 5200) after some modifications to the optics and electronics to reduce the sensor noise in the optical beam deflection sensor [31]. A multifunction data acquisition device (National Instruments: NI USB–6366) was used to acquire the realtime waveform from the deflection sensor, and the thermal noise spectrum was computed by the fast Fourier transform (FFT) algorithm.

We used a Si cantilever with a backside Al coating (Nanosensors: PPP-ZEILR). We first measured the thermal noise spectrum of the first free resonance in air and it was fitted to the SHO model [31, 32], to determine the first free resonance frequency ($f_0 = 26.1$ kHz) and the quality factor ($Q_0 = 140$), from which the spring constant of the cantilever (k_z) was calibrated by Sader's method to be 1.2 N/m [33]. We also calibrated the angular deflection

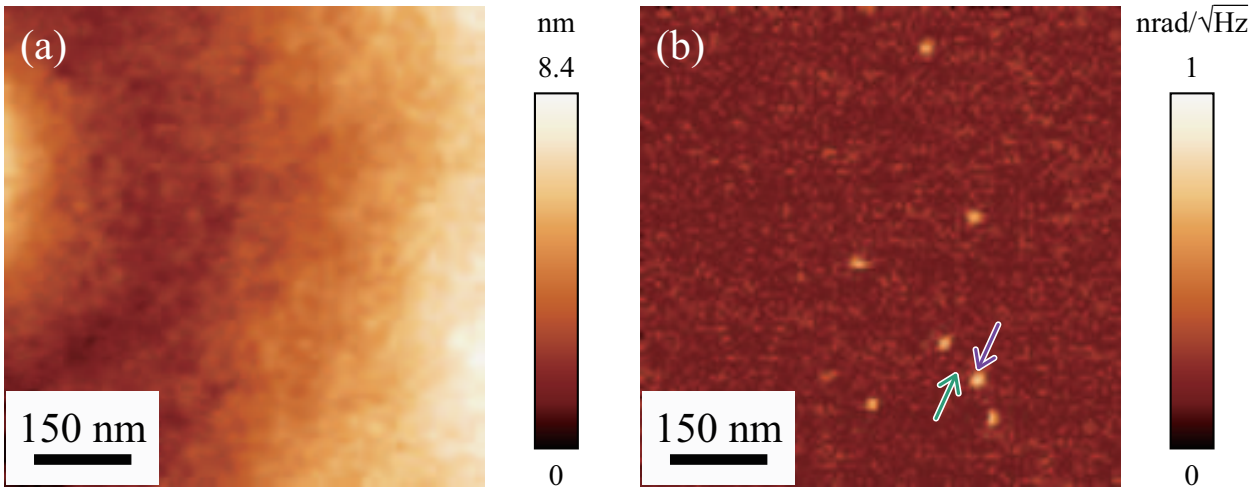

FIG. 2: (color online) STNM images of photopolymer film with Au nanoparticles buried at a depth of 300 nm. The images are shown after trimming of an area of 780 nm × 780 nm (100 × 100 pixels. (a) Topographic image showing a featureless photopolymer surface. (b) Noise magnitude image reconstructed at 104.2 kHz showing buried Au nanoparticles as bright spots. The thermal noise spectra recorded at the locations indicated by the arrows are shown in Fig. 3.

sensitivity of the optical beam deflection sensor (See Supplementary Information A).

We brought the tip into contact with the sample surface at a loading force of 10 nN, and performed AFAM imaging at the first contact resonance using a piezoelectric plate glued to the polyimide sheet and a lock-in amplifier (Zurich Instruments: HF2LI), and found some subsurface Au nanoparticle features (See Supplementary Information B for the details of the AFAM imaging). We then performed STNM imaging on the same area. While the tip was scanning the surface, a realtime waveform of the cantilever deflection was recorded at each pixel for 625 ms with a sampling frequency of 400 kHz. The waveform consisting of 250,000 data points was divided into 25 segments of 10,000 data points each. The thermal noise spectrum was calculated from each segmented waveform by the FFT algorithm, and the averaged thermal noise spectrum was obtained. The frequency resolution was 40 Hz. The total data acquisition time for two STNM images (trace and retrace) with 128 × 128 pixels each was about 6 h.

Figure 2(a) is a topographic image, which was obtained during STNM measurement, showing a smooth featureless surface of the top-coat layer. Since we collected the thermal noise spectrum at each pixel, we can reconstruct the STNM noise magnitude image of an arbitrary frequency in the frequency range of concern. Figure 2(b) is an STNM noise

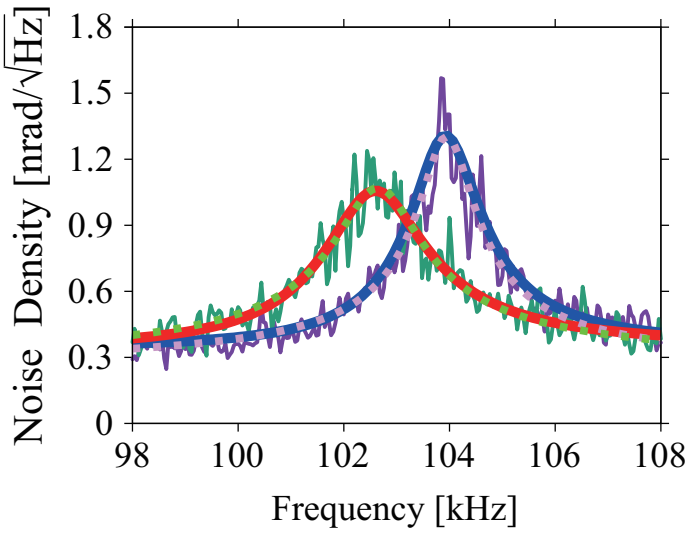

FIG. 3: (color online) Thermal noise spectra recorded on the photopolymer surface on an area with (purple) and without (green) a buried Au nanoparticle. The dashed and solid curves are fitted theoretical curves using Eqs. (1) and (3), respectively.

magnitude image at 104.2 kHz, which shows the bright features at the same locations as those in the AFAM phase image (See Supplementary Information B). The figure clearly shows well-dispersed Au nanoparticles buried 300 nm into the polymer matrix, as well as those presented in the previous papers[3, 15, 24], while there are no features at the same locations in the topographic image in Fig. 2(a).

Figure 3 shows the thermal noise spectra measured on the pixels indicated by the arrows in Fig. 2(b); the purple and green curves are the thermal noise spectra with and without the buried Au nanoparticle underneath, respectively. Unlike AFAM and other conventional techniques that utilize the piezoelectric actuator for excitation, the thermal noise spectrum measured by STNM is free from spurious resonance peaks and skewness caused by the nonlinear oscillations. We again fitted the thermal noise spectra by the SHO model,

$$N_\theta^{f_c} = \sqrt{\frac{P_{\rm peak}}{{Q_c}^2[1-(f/f_c)^2]^2+(f/f_c)^2} + {n_\theta}^2}, \tag{1}$$

to determine the contact resonance frequency (f_c) and the quality factor (Q_c). $P_{\rm peak}$ is a fitting parameter corresponding to the peak noise power density of the angular deflection of the cantilever. As shown in Fig. 3, the thermal noise spectra were well fitted by Eq. (1) as the dashed curves, and we found that f_c and Q_c on the area with the Au nanoparticle were

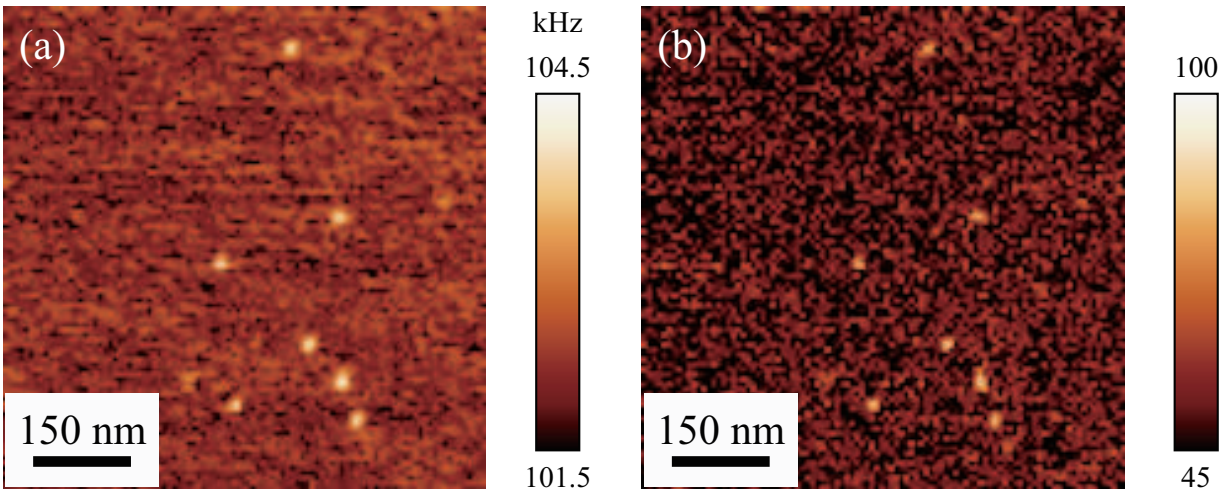

FIG. 4: (color online) (a) Contact resonance frequency (f_c) and (b) quality factor (Q_c) images of the photopolymer film with buried Au nanoparticles. Bright features correspond to the Au nanoparticles buried 300 nm below the photopolymer surface.

shifted to about 104.0 kHz and 77 from the values on the area without it, which were about 102.7 kHz and 53, respectively. We calculated f_c and Q_c using the same method for all the thermal noise spectra, from which we reconstructed the f_c and Q_c images as shown in Figs. 4(a) and 4(b), respectively. We can now see the bright features that represent the subsurface Au nanoparticles both in the f_c and Q_c images, as clearly as in Fig. 2(b). Roughly speaking, f_c and Q_c are related to the contact stiffness and inverse of the damping.

Since STNM does not require external excitation methods, the subsurface contrasts are not contributed by the surface acoustic standing wave. The variation in the surface viscoelastic properties, namely, the contact stiffness and damping, should play a significant role. In the following section, we assess the difference between the surface viscoelastic properties on the area with a buried Au nanoparticle and those on the area without it.

We analyzed the thermal noise spectra using a linear spring dashpot model, i.e., the cantilever end is connected to the sample surface with a spring of k^* in parallel with a dashpot with damping γ (Voigt model, See Supplementary Information C) [22, 34]. We derived a fitting function for the thermal noise spectrum based on the frequency response function of the cantilever under the boundary conditions for the AFAM, in which the sample surface is excited, to determine k^* and γ (See Supplementary Information C). We assume the thermal noise magnitude at the contact resonance is proportional to the angular deflection at the cantilever end induced by a unit sample surface oscillation, that is, a frequency response

function for the angular deflection is given by

$$\theta_z^{\mathrm{STNM}}(\kappa) = \kappa\phi(\kappa)\frac{\sin(\kappa L)\sinh(\kappa L)}{N(\kappa)}, \tag{2}$$

where κ and L are a wave number and the length of the cantilever, respectively. κ is related to the oscillation frequency (f) by $\kappa = \kappa_1\sqrt[4]{(f/f_0)^2 - if/(f_0Q_0)}$, where κ_1, f_0, and Q_0 are the wave number ($= 1.8751/L$), frequency, and quality factor of the first free resonance. $\phi(\kappa)$ and $N(\kappa)$ are given by $\phi(\kappa) = 3[k^* + i(2\pi f_0)(\kappa/\kappa_1)^2\gamma]/k_z$ and $N(\kappa) = (\kappa L)^3(1 + \cos\kappa L\cosh\kappa L) - \phi(\kappa)(\cos\kappa L\sinh\kappa L - \sin\kappa L\cosh\kappa L)$, respectively. We derived the fitting function for the thermal noise spectrum obtained by the STNM as

$$N_\theta^{f_c} = \sqrt{|\theta_z^{\mathrm{STNM}}(\kappa)u_{\mathrm{th}}|^2 + {n_\theta}^2}, \tag{3}$$

where u_{th} is a fitting parameter corresponding to the thermal noise displacement at the cantilever end. We fitted the thermal noise spectra in Fig. 3 with Eq. (3). The red and blue curves in Fig. 3 show the best fitted curves to the measured spectra (green and purple curves). Based on the fitting parameters, k^* and γ on the area above the Au nanoparticle were 63 N/m and 5.1 $\times 10^{-6}$ Ns/m, respectively, while those on the area without it were 55 N/m and 6.1 $\times 10^{-6}$ Ns/m, respectively. Therefore, k^* was increased by 15 % and γ was decreased by about 16 % due to the presence of the Au nanoparticle in the matrix. Thus the imaging mechanism of the Au nanoparticles by STNM is quantitatively explained by the increase in the contact stiffness and damping of the polymer surface due to the existence of the Au nanoparticle. Based on the fitting parameters, the magnitude of the thermal displacement of the tip can also be estimated as about 3.3 pm and 4.2 pm on the area with and without the buried Au nanoparticle, respectively (See Supplementary information D). Note that we also calculated k^* and γ using another fitting function based on the other boundary condition; i.e., a concentrated force is applied at the cantilever end, and obtained almost the same results.

We now discuss why the Au nanoparticles buried at such a depth can influence the surface stiffness and damping and eventually change the boundary conditions. We considered two extreme cases; the sphere-plane contact models [35] and one-dimensional model to calculate the variation in k^*. We first considered the AFM cantilever tip in contact with an elastic

surface in which k^* is defined as $dF_\mathrm{n}/d\delta$, where δ and F_n are the surface displacement and normal loading force, respectively. Under the Hertzian model (no adhesion), δ_Hertz is given by $a_\mathrm{Hertz}^2/R_\mathrm{t}$, where a_Hertz is the contact tip radius given by $a_\mathrm{Hertz} = [3R_\mathrm{t}F_\mathrm{n}/(4E^*)]^{1/3}$ where R_t and E^* are the tip radius and reduced Young's modulus, respectively. Using these relationships, E^* is related to k^* as $E^* = \sqrt{k^{*3}/(6R_\mathrm{t}F_\mathrm{n})}$. By assuming R_t = 15 nm and F_n =10 nN, E^* on the area with and without the Au nanoparticle were calculated as 16.7 GPa and 13.5 GPa, respectively, from the k^* value obtained by the STNM measurement. E^* is related to the effective sample stiffness (E_s) by $E^* = [(1-\nu_\mathrm{t}^2)/E_\mathrm{t} + (1-\nu_\mathrm{s}^2)/E_\mathrm{s}]^{-1}$, where E_t denotes the Young's moduli of the tip (= 130 GPa)[21], and ν_t (= 0.18) [21] and ν_s(= 0.33) [36] are the Poisson's ratios of the tip and sample, respectively. Therefore, E_s value on the area with and without the Au nanoparticle were calculated to be 16.7 GPa and 13.5 GPa, respectively. These values are much larger than the Young's modulus of the top-coat photopolymer film in the literature [36] and that experimentally determined (E_tc = 3.4 GPa) (See Supplementary information E). Moreover, the Hertzian model predicts that the stress field extends to a depth of about $3a_\mathrm{Hertz}$[35, 37]. Since a_Hertz was about 2 nm in the present case, it is not expected that the effective sample stiffness is affected by the Au nanoparticle buried 300 nm from the surface based on the Hertzian contact model.

We also considered the Johnson-Kendall-Roberts (JKR) contact model[35], in which the adhesion force was taken into account. In the JKR model, δ_JKR and $a_\mathrm{JKR}*$ are given by $\delta_\mathrm{JKR} = a_\mathrm{JKR}{*}^2/R_\mathrm{t} - 2\sqrt{a_\mathrm{JKR}*F_\mathrm{ad}/(R_\mathrm{t}E^*)}$ and $a_\mathrm{JKR}* = [3R_\mathrm{t}\left(F_\mathrm{n} + 2F_\mathrm{ad} + \sqrt{4F_\mathrm{n}F_\mathrm{ad} + 4{F_\mathrm{ad}}^2}\right)/(4E^*)]^{1/3}$, respectively, where F_ad (= 15 nN) is the adhesion force. Based on the JKR model, E^* on the area with and without the Au nanoparticle were calculated to be 11 GPa and 9 GPa, respectively, from which the E_s values were 10.6 GPa and 8.6 GPa, respectively. This calculation suggests that the Young's modulus on the top-coat photopolymer was increased by about 23%. Note that these values are close to the Young's modulus of the top-coat photopolymer film in the literature [36], but still greater than the experimental value. Although we consider that the contact condition in the present study is more correctly described by the JKR contact model than by the Hertzian model, $a_\mathrm{JKR}*$ by the JKR model was still as low as about 4.5 nm, and it does not account for the variation in the contact stiffness by the deeply buried Au nanoparticle.

Although the JKR model qualitatively explained the contact stiffness variation, it failed to explain the depth range of the subsurface imaging since the expected elastic stress field

was on the order of 10 nm. We finally noted that we found that the effective Young's modulus could be reproduced by considering a one-dimensional model. We modeled the sample as a two-layer film of the top-coat layer and the Au layer. The variation in thickness of the two-layer film (δ_{1D}) under a uniform stress (σ) is given by $\delta_{1D} = (\sigma/E_{tc})t_{tc} + (\sigma/E_{Au})t_{Au}$, where t_{tc}, t_{Au}, E_{tc}, and E_{Au} denote the top-coat photopolymer thickness, Au nanoparticle diameter, and the Young's modulus of the top-coat film and Au (= 79 GPa [38]), respectively. The effective Young's modulus of the multilayer film can now be calculated as $E_s^{1D} = (\sigma/\delta_{1D})(t_{tc} + t_{Au})$. Assuming E_{tc} as 3.4 GPa, the one-dimensional model predicts that Young's modulus on the top-coat photopolymer was increased by about 15%, which was consistent with the variation predicted by the STNM measurements and the JKR contact model (23%). Therefore, we interpreted the subsurface contrasts in the experimental results by STNM as well as by AFAM as the variation in the contact stiffness and damping because the stress field extends more than expected from the sphere-plane contact models up to several hundreds of nm. This may be possible due to the anisotropy in the viscoelastic property of the spin-coated photopolymer film and some nonlinear or nanometer-scale effects that have not been considered in the macroscopic contact models. The conclusion is also consistent with the previous studies that explained the subsurface imaging mechanisms using one-dimensional models [39–41]. Further theoretical and experimental studies are necessary to comprehend the imaging mechanisms.

In conclusion, we experimentally performed the visualization of subsurface features by STNM that simply measures the thermal noise spectrum without additional excitation methods. We realized an ultimate simplification of the measurement scheme and imaged the Au nanoparticles buried 300 nm in the photopolymer matrix in the least invasive way. We have shown that the subsurface features in the STNM images were brought by the variation in the contact stiffness and damping by the fitting of the theoretical equation to the thermal noise spectra. It was also shown, based on the JKR contact model, that the Young's modulus of the photopolymer surface was increased by 23% due to the presence of the Au nanoparticle. However, the contact models failed to explain the imaging mechanisms because the depth of the stress field in the model was more shallow than the depth of the Au nanoparticle. On the other hand, the simple one-dimensional model also predicted the increase in the Young's modulus of the photopolymer film by 15%. Therefore, we suggest that the imaging of subsurface features is realized by the stress field extension in a quasi-one-dimensional manner. To

investigate the detailed one-dimensional strain model, the relationship between the effective Young's modulus of the top-coat polymer film and the top-coat thickness will be examined in the near future. As shown by the STNM experiments, the subsurface features could be solely explained by considering the variation in the viscoelastic properties of the area under the tip. Therefore, the subsurface imaging mechanisms of various experimental schemes using the contact resonance might need to be revisited. The STNM technique will serve as a technique to study subsurface imaging mechanisms by the AFM related techniques as well as a method to quantitatively evaluate the viscoelastic properties of the sample surface.

This study was supported by a Grant-in-Aid for JSPS Fellows (No. 26462) and a Grant-in-Aid for Challenging Exploratory Research (No. 16K13686) from Japan Society for the Promotion of Science.

* Electronic address: keicoba@iic.kyoto-u.ac.jp

[1] K. Yamanaka, H. Ogiso, and O. Kolosov, Applied Physics Letters **64**, 178 (1994).

[2] H. Bodiguel, H. Montes, and C. Fretigny, Review of Scientific Instruments **75**, 2529 (2004).

[3] G. S. Shekhawat and V. P. Dravid, Science **310**, 89 (2005).

[4] L. Tetard, A. Passian, K. T. Venmar, R. M. Lynch, B. H. Voy, G. Shekhawat, V. P. Dravid, and T. Thundat, Nature Nanotechnology **3**, 501 (2008).

[5] L. Tetard, A. Passian, R. M. Lynch, B. H. Voy, G. Shekhawat, V. Dravid, and T. Thundat, Applied Physics Letters **93**, 133113 (2008).

[6] K. Yamanaka, K. Kobari, and T. Tsuji, Japanese Journal of Applied Physics **47**, 6070 (2008).

[7] Z. Parlak and F. L. Degertekin, Journal of Applied Physics **103**, 114910 (2008).

[8] G. Shekhawat, A. Srivastava, S. Avasthy, and V. Dravid, Applied Physics Letters **95**, 263101 (2009).

[9] M. Ashino, R. Wiesendanger, A. N. Khlobystov, S. Berber, and D. Tománek, Physical Review Letters **102**, 195503 (2009).

[10] L. Tetard, A. Passian, R. Farahi, and T. Thundat, Ultramicroscopy **110**, 586 (2010).

[11] L. Tetard, A. Passian, and T. Thundat, Nature Nanotechnology **5**, 105 (2010).

[12] L. Tetard, A. Passian, S. Eslami, N. Jalili, R. Farahi, and T. Thundat, Physical Review Letters **106**, 180801 (2011).

[13] S. Hu, C. Su, and W. Arnold, Journal of Applied Physics **109**, 084324 (2011).

[14] J. P. Killgore, J. Y. Kelly, C. M. Stafford, M. J. Fasolka, and D. C. Hurley, Nanotechnology **22**, 175706 (2011).

[15] K. Kimura, K. Kobayashi, K. Matsushige, and H. Yamada, Ultramicroscopy **133**, 41 (2013).

[16] D. Ebeling, B. Eslami, and S. D. J. Solares, ACS Nano **7**, 10387 (2013).

[17] G. Verbiest, T. Oosterkamp, and M. Rost, Nanotechnology **24**, 365701 (2013).

[18] P. Vitry, E. Bourillot, C. Plassard, Y. Lacroute, L. Tetard, and E. Lesniewska, Applied Physics Letters **105**, 053110 (2014).

[19] G. Verbiest and M. Rost, Nature Communications **6**, 1 (2015).

[20] G. Verbiest, J. Simon, T. Oosterkamp, and M. Rost, Nanotechnology **23**, 145704 (2012).

[21] U. Rabe, K. Janser, and W. Arnold, Review of Scientific Instruments **67**, 3281 (1996).

[22] U. Rabe, in *Applied Scanning Probe Methods II* (Springer, 2006) pp. 37–90.

[23] A. Striegler, B. Koehler, B. Bendjus, M. Roellig, M. Kopycinska-Mueller, and N. Meyendorf, Ultramicroscopy **111**, 1405 (2011).

[24] K. Kimura, K. Kobayashi, A. Yao, and H. Yamada, Nanotechnology **27**, 415707 (2016).

[25] F. Benmouna and D. Johannsmann, Langmuir **20**, 188 (2004).

[26] P. Vairac, B. Cretin, and A. J. Kulik, Applied Physics Letters **83**, 3824 (2003).

[27] F. Benmouna, T. D. Dimitrova, and D. Johannsmann, Langmuir **19**, 10247 (2003).

[28] M. Gelbert, A. Roters, M. Schimmel, J. Rühe, and D. Johannsmann, Surface and Interface Analysis **27**, 572 (1999).

[29] A. Roters and D. Johannsmann, Journal of Physics: Condensed Matter **8**, 7561 (1996).

[30] J. Cleveland, T. Schäffer, and P. Hansma, Physical Review B **52**, R8692 (1995).

[31] T. Fukuma, M. Kimura, K. Kobayashi, K. Matsushige, and H. Yamada, Review of Scientific Instruments **76**, 053704 (2005).

[32] P. R. Saulson, Phys. Rev. D **42**, 2437 (1990).

[33] J. H. Sader, J. W. M. Chon, and P. Mulvaney, Review of Scientific Instruments **70**, 3967 (1999).

[34] P. Yuya, D. Hurley, and J. A. Turner, Journal of Applied Physics **104**, 074916 (2008).

[35] K. L. Johnson and K. L. Johnson, *Contact mechanics* (Cambridge university press, 1987).

[36] L. Calabri, N. Pugno, A. Rota, D. Marchetto, and S. Valeri, Journal of Physics: Condensed Matter **19**, 395002 (2007).

[37] U. Rabe, S. Amelio, M. Kopycinska, S. Hirsekorn, M. Kempf, M. Göken, and W. Arnold, Surface and Interface Analysis **33**, 65 (2002).

[38] D. Dowson, C. M. Taylor, and M. Godet, *Mechanics of coatings*, Vol. 17 (Elsevier, 1990).

[39] A. F. Sarioglu, A. Atalar, and F. L. Degertekin, Applied Physics Letters **84**, 5368 (2004).

[40] J. H. Cantrell and S. A. Cantrell, Physical Review B **77**, 165409 (2008).

[41] S. A. Cantrell, J. H. Cantrell, and P. T. Lillehei, Journal of Applied Physics **101**, 114324 (2010).

Supplementary Information

Visualization of Au Nanoparticles Buried in a Polymer Matrix by Scanning Thermal Noise Microscopy

Supplementary Information A: Thermal Noise Spectrum of First Free Resonance

Figure S1 shows a thermal noise spectrum of the first free resonance of the cantilever used for imaging of buried Au nanoparticles by STNM in the present study. We fitted the measured thermal noise (voltage) spectrum ($N_{\mathrm{v}}^{f_0}$) to the equation for that of the simple harmonic oscillator (SHO) [S1], given by

$$N_{\mathrm{v}}^{f_0} = S_z N_z^{f_0} = S_z \sqrt{\frac{2k_{\mathrm{B}}T}{\pi f_0 k_z Q_0} \frac{1}{[1-(f/f_0)^2]^2 + [f/(f_0 Q_0)]^2} + {n_z}^2}, \tag{S1}$$

where S_z and n_z are a sensitivity of the optical beam deflection sensor to the displacement and a noise-equivalent displacement density, respectively. We first fitted the thermal noise spectrum to Eq. (S1) with the nominal value of k_z and determined f_0 and Q_0, from which we calibrated k_z by Sader's method [S2]. Then we fitted the spectrum again to Eq. (S1) with the calibrated k_z to determine S_z (= 25 mV/nm) and n_z (= 77 fm/$\sqrt{\mathrm{Hz}}$) [S3].

Since the voltage output signal of the optical beam deflection sensor is proportional to the angular deflection frequency rather than the displacement of the cantilever, it is reasonable to rewrite Eq. (S1) as

$$N_{\mathrm{v}}^{f_0} = S_\theta N_\theta^{f_0} = S_\theta \sqrt{{\theta_z^{f_0}}^2 \frac{2k_{\mathrm{B}}T}{\pi f_0 k_z Q_0} \frac{1}{[1-(f/f_0)^2]^2 + [f/(f_0 Q_0)]^2} + {n_\theta}^2}, \tag{S2}$$

where S_θ and n_θ are a sensitivity of the optical beam deflection sensor to the angular deflection and a noise-equivalent angular deflection density, respectively. $\theta_z^{f_0}$ is a conversion factor of the displacement to the angular deflection at the first free resonance (= $1.3765/L$), where L denotes the length of the cantilever (= 450 μm). Since S_θ is related to S_z by $S_\theta = S_z/\theta_z^{f_0}$, S_θ (= 8,170 V/rad) and n_θ (= 0.24 nrad/$\sqrt{\mathrm{Hz}}$) were readily determined.

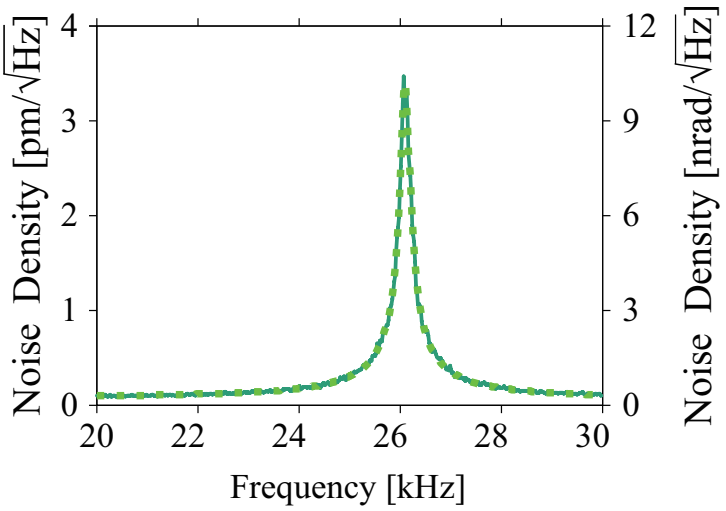

FIG. S1: Thermal noise spectrum of the first free resonance of the cantilever. The solid and dashed curves are the measured spectrum and the theoretical curve fitted with Eq. (S1), respectively.

Supplementary Information B: AFAM Phase Imaging

Figure S2 shows an atomic force acoustic microscopy (AFAM) phase image of a photopolymer film with Au nanoparticles buried 300 nm in depth. An excitation signal of 99.6 kHz with an amplitude of 8.5 mV was applied to a piezoelectric actuator glued to the backside of the polyimide sheet. See Ref. [S4] for the details of the AFAM experimental setup. The image area is the same as those of Figs. 2 and 4.

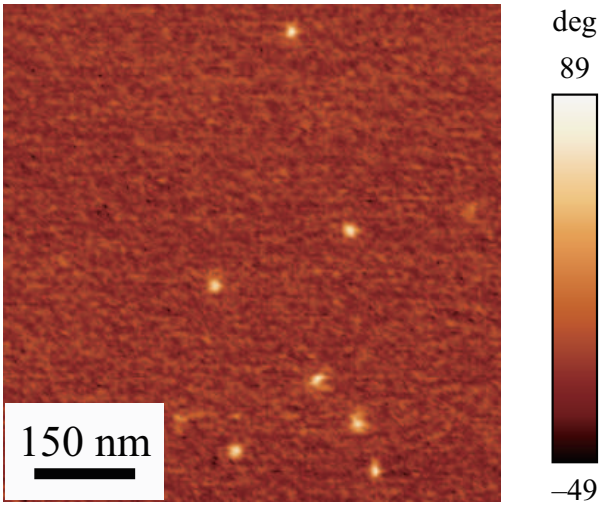

FIG. S2: AFAM phase image of a photopolymer film with Au nanoparticles buried 300 nm in depth.

Supplementary Information C: Fitting Function for Thermal Noise Spectrum of STNM

We derive a fitting function for the thermal noise spectrum of the contact resonance based on the frequency response function of AFAM. The tip-sample interaction is modeled by a linear spring dashpot model, i.e., the cantilever end is connected to the sample surface with a spring and a dashpot, representing the contact stiffness (k^*) and damping (γ), respectively, as shown in Fig. S3. The equation of motion for damped flexural oscillation of the cantilever is given by

$$EI\frac{\partial^4 y}{\partial x^4} + \eta\rho S\frac{\partial y}{\partial t} + \rho S\frac{\partial^2 y}{\partial x^2} = 0 \tag{S3}$$

where E is the Young's modulus of the cantilever, ρ is its mass density, S is the area of its cross section, I is the area moment of inertia, and η is a damping constant. y represents the deflection of the cantilever in its thickness direction at the position of x, which is a coordinate in length direction of the cantilever [S5]. The mode shape function, $y(x)$, can be expressed as

$$y(x) = A_1(\cos\kappa x+\cosh\kappa x)+A_2(\cos\kappa x-\cosh\kappa x)+A_3(\sin\kappa x+\sinh\kappa x)+A_4(\sin\kappa x-\sinh\kappa x) \tag{S4}$$

where A_1, A_2, A_3, and A_4 denote constants and κ is a wave number. The boundary conditions for AFAM are

$$y(0) = 0 \text{ and} \tag{S5}$$

$$y'(0) = 0 \tag{S6}$$

for the cantilever base ($x = 0$), and

$$y''(L) = 0 \text{ and} \tag{S7}$$

$$y'''(L) = \frac{\phi(\kappa)}{L^3}\left[y(L) - u_0\right] \tag{S8}$$

for the cantilever end ($x = L$), where u_0 is an oscillation amplitude of the sample surface. $\phi(\kappa)$ is a contact function given by

$$\phi(\kappa) = \frac{3}{k_z}(k^* + i\omega\gamma) = 3\left[\frac{k^*}{k_z} + i(\kappa L)^2 \frac{2\pi\gamma f_0}{(1.8751)^2 k_z}\right], \tag{S9}$$

where ω is an angular frequency ($= 2\pi f$). By calculating the constants A_1, A_2, A_3, and A_4, $y(x)$ is obtained as

$$\begin{aligned} y(x) &= -\frac{u_0}{2}\phi(\kappa)\frac{\sin\kappa L + \sinh\kappa L}{N(\kappa)}(\cos\kappa x - \cosh\kappa x) \\ &+ \frac{u_0}{2}\phi(\kappa)\frac{\cos\kappa L + \cosh\kappa L}{N(\kappa)}(\sin\kappa x - \sinh\kappa x), \end{aligned} \tag{S10}$$

with $N(\kappa)$ given by

$$N(\kappa) = (\kappa L)^3(1 + \cosh\kappa L\cos\kappa L) - \phi(\kappa)(\sinh\kappa L\cos\kappa L - \cosh\kappa L\sin\kappa L). \tag{S11}$$

Since we use the optical beam deflection sensor, whose output signal is proportional to the angular deflection of the cantilever, we also calculate the derivative of the mode shape function as

$$\begin{aligned} y'(x) &= \kappa\frac{u_0}{2}\phi(\kappa)\frac{\sin\kappa L + \sinh\kappa L}{N(\kappa)}(\sin\kappa x + \sinh\kappa x) \\ &+ \kappa\frac{u_0}{2}\phi(\kappa)\frac{\cos\kappa L + \cosh\kappa L}{N(\kappa)}(\cos\kappa x - \cosh\kappa x). \end{aligned} \tag{S12}$$

By substituting x with L for these equations, the oscillation amplitude of the displacement and the angular deflection at the cantilever end for AFAM are obtained as

$$y_{\mathrm{AFAM}}(L) = u_0\phi(\kappa)\frac{\sin\kappa L\cosh\kappa L - \sinh\kappa L\cos\kappa L}{N(\kappa)} \tag{S13}$$

and

$$y'_{\mathrm{AFAM}}(L) = \kappa u_0\phi(\kappa)\frac{\sin\kappa L\sinh\kappa L}{N(\kappa)}, \tag{S14}$$

respectively. Here we define a frequency response function of the angular deflection for STNM, namely the angular deflection amplitude of the cantilever end induced by a unit

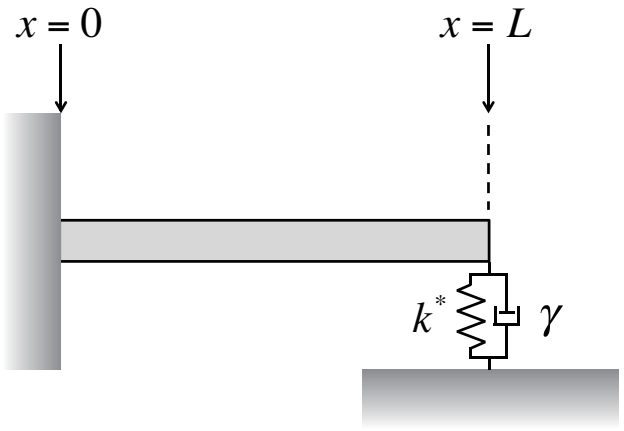

FIG. S3: Schematic of a cantilever interacting with a sample surface. The tip-sample interaction is modeled by a linear spring dashpot model (Voigt model).

sample surface oscillation as

$$\theta_z^{\mathrm{STNM}}(\kappa) = \frac{y'_{\mathrm{AFAM}}(\kappa)}{u_0} = \kappa\phi(\kappa)\frac{\sin(\kappa L)\sinh(\kappa L)}{N(\kappa)}. \tag{S15}$$

Supplementary Information D: Magnitude of Thermal Displacement of Tip

By inserting the best fitting parameters for k^* and γ to Eq. (S13) and replacing u_0 with u_{th} obtained by the fitting, we can recover the magnitude of the displacement density of

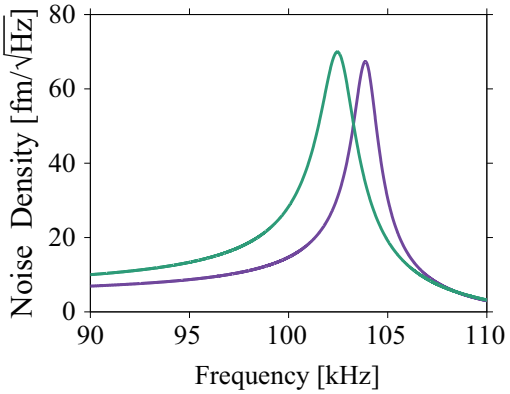

FIG. S4: (color online) Theoretical thermal noise spectrum of the tip calculated using the best fitting parameters for fitting Eq. (3) to the curves in Fig. 3. The purple and green curves show theoretical curves on the photopolymer surface areas with and without a buried Au nanoparticle using Eq. (S13).

the cantilever end (tip) as shown in Fig S4. The magnitude of the thermally driven tip oscillation at the first contact resonance was estimated as about 3.3 pm and 4.2 pm on the photopolymer surface areas with and without the buried Au nanoparticle, respectively.

Supplementary Information E: Young's Modulus of Photopolymer Film

We fabricated a patterned photopolymer film on the polyimide sheet, with a thickness of 250 nm, by photolithography, and performed STNM measurement at the edge of the film. Fig. S5 shows the thermal noise spectra of the contact resonance of the cantilever recorded on the areas on the photopolymer film and the polyimide sheet. The purple and green curves are a typical thermal noise spectrum on the photopolymer film and that on the polyimide sheet, respectively. As we could not find a significant difference in the resonance frequency or quality factor, we consider that the Young's modulus of the photopolymer film used in this study is almost the same as that of the polyimide sheet (= 3.4 GPa), which is found in the literature [S6].

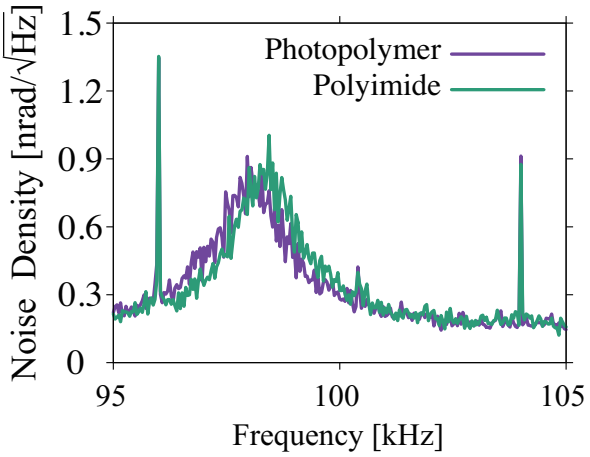

FIG. S5: (color online) Typical thermal noise spectra recorded on the photopolymer film surface and the polyimide sheet.

---

* Electronic address: keicoba@iic.kyoto-u.ac.jp

[S1] P. R. Saulson, Phys. Rev. D **42**, 2437 (1990).

[S2] J. H. Sader, J. W. M. Chon, and P. Mulvaney, Review of Scientific Instruments **70**, 3967 (1999).

[S3] J. L. Hutter and J. Bechhoefer, Review of Scientific Instruments **64**, 1868 (1993).

[S4] K. Kimura, K. Kobayashi, K. Matsushige, and H. Yamada, Ultramicroscopy **133**, 41 (2013).

[S5] U. Rabe, in *Applied Scanning Probe Methods II* (Springer, 2006) pp. 37–90.

[S6] *Mechanical property of polyimide sheet (in Japanese)* (DuPont-Toray co., ltd.) `http://www.td-net.co.jp/kapton/sort/hv_type/machine.html`.